



Crustal structure and thickness along the Yellowstone hot spot track: Evidence for lower crustal outflow from beneath the eastern Snake River Plain

Huaiyu Yuan

Department of Earth Science, University of California, Berkeley, California 94720, USA

Ken Dueker and Josh Stachnik

*Department of Geology and Geophysics, University of Wyoming, Laramie, Wyoming 82071, USA
(dueker@uwyo.edu)*

[1] Receiver functions from seismic stations about the Yellowstone hot spot track are migrated to depth using a V_p/V_s map constructed from stacking of the direct and free surface Moho reverberations (i.e., H-K analysis) and a shear velocity tomogram constructed from surface wave measurements. The thickest crust (48–54 km) resides in the Wyoming province beneath the sampled Laramide age blocks, and the thinnest crust (32–37 km) resides in the Montana Basin and Range province. The eastern Snake River Plain (ESRP) crust is thickest (47 km) at its NE end beneath the young calderas and thinnest (40 km) at its SW end beneath the older Twin Falls caldera. Two ESRP crustal thickness domains are found: (1) at the older Twin Falls and Picabo calderas, the mean ESRP crust is 4 km thicker with respect to its margins and (2) adjacent to the Heise caldera field, the mean ESRP crust is 4 km thicker with respect to its SE margin crust but no thicker with respect to its NW margin crust. This lobe of anomalously thick crust is explained as resulting from lower crustal outflow from beneath the Heise caldera field. Confirmation of these crustal thickness variations is provided by inspection of common conversion point (CCP) stacks that delineate several secondary features: the top of a thick high-velocity (3.9 km/s) lower crust layer within the Wyoming province up to 17 km thick and a paired negative and positive amplitude arrival at 12 km depth and 18 km depth beneath the Yellowstone Caldera. This paired arrival would be consistent with a low-velocity zone perhaps associated with magma staging beneath the caldera. Our most important finding is that the magmatic loads injected into the ESRP crust over the last 4–12 Myr, in tandem with the ESRP crustal viscosity structure, have been sufficient to drive significant outflow of the ESRP lower crust.

Components: 6797 words, 12 figures.

Keywords: Yellowstone; crust hot spot.

Index Terms: 7203 Seismology: Body waves (1219); 7205 Seismology: Continental crust (1219).

Received 18 August 2009; **Revised** 1 December 2009; **Accepted** 7 December 2009; **Published** 13 March 2010.

Yuan, H., K. Dueker, and J. Stachnik (2010), Crustal structure and thickness along the Yellowstone hot spot track: Evidence for lower crustal outflow from beneath the eastern Snake River Plain, *Geochem. Geophys. Geosyst.*, 11, Q03009, doi:10.1029/2009GC002787.

1. Introduction

[2] The Yellowstone hot spot track manifests a sequence of calderas that begin 16.9 Myr ago near the tristate region of Oregon-Idaho-Nevada with the calderas propagating to the NE (Figure 1). The sequence of calderas trend to the NE from the Bruneau-Jarbridge (12.7–10.5 Ma) to the Twin Falls (10.5–8.6 Ma) to the Picabo (10.2–9.2 Ma) to the Heise (6.6–4.4 Ma) caldera fields. All together, these calderas reside within the structural downwarp termed the eastern Snake River Plain (ESRP) [Perkins and Nash, 2002; Bonnicksen et al., 2007; Anders, 2009; Rodgers and McCurry, 2009; Leeman et al., 2008]. The most recent 2.1–0.6 Ma Huckleberry Ridge, Island Park, and Yellowstone calderas reside primarily upon the Yellowstone Plateau. Explanation of the ESRP downwarp requires knowledge of the crustal magma injection volumes and composition, time-integrated extension, and time-integrated lower crustal flow fluxes [McQuarrie and Rodgers, 1998; Stachnik et al., 2008; Rodgers and McCurry, 2009]. The largest uncertainty with respect to calculating an ESRP crustal mass balance is knowledge of the pre-hot spot magmatism and extension and the crustal thickness and density. The pre-hot spot conditions can only be roughly estimated from the tectonic history of this region [Hamilton, 1989; Dickinson, 2006; Foster et al., 2006]. However, the modern day crustal thickness and density structure can be estimated from the combination of the Earthscope Transportable array and previous PASSCAL seismic data.

[3] Previous petrologic and geochemical modeling suggests that 8–14 km of basaltic magma was injected primarily into the 8–18 km depth range beneath the individual calderas [Bonnicksen et al., 2007; Hanan et al., 2008; McCurry and Rodger, 2009; Leeman et al., 2008]. Heat budget modeling of the duration and volumes of the Rhyolite eruption volumes also requires about 10 km of basaltic magma injection into the mid to upper crust [Leeman et al., 2008]. The midcrust is the preferred Mixing-Assimilation-Hybridization (MASH) region where the Rhyolitic liquids are distilled via fractionation and modest levels of crustal assimilation [Hildreth and Moorbath, 1988]. Geophysical evidence for the fossil (crystallized and cooled) midcrustal MASH zone beneath the ESRP derives from gravity analysis [Sparlin et al., 1982; Lowry and Smith, 1995; Lowry et al., 2000; DeNosaquo et al., 2010], seismic refraction analysis [Smith et al., 1982; Sparlin et al., 1982], and local earth-

quake analysis [DeNosaquo et al., 2010]. In addition, our surface wave seismic tomogram finds an approximately 10 km thick high-velocity layer in the ESRP midcrust with the top of the high-velocity layer at 15–25 km depth [Stachnik et al., 2008].

[4] As the magma injections beneath the calderas cool on 1–2 Myr time scales [Anders and Sleep, 1992], the midcrustal sill complex (MCS) is predicted to become denser than the surrounding country rocks [McCurry and Rodger, 2009; DeNosaquo et al., 2010]. This high-density MCS would thus become a positive load on the lower crust which could force the lower crust to flow outward on million year time scales if the crustal viscosity is sufficiently low [Buck, 1991; McQuarrie and Rodgers, 1998; Royden et al., 2008]. The ESRP can thus be viewed as a magmatic time machine that loads the lower crust; this factor permits assessment of potential lower crustal flow if accurate crustal thickness maps are available.

2. Data and Methods

[5] The broadband seismic recording analyzed (Figure 1) derive from Earthscope Transportable array data, six three-component short-period University of Utah Seismic Network seismometers in Yellowstone Park and five dominantly broadband PASSCAL seismic experiments: the 1993 eastern Snake River Plain line array [Saltzer and Humphreys, 1997], the N–S and NW–SE Deep Probe passive line arrays [Dueker and Yuan, 2004], the 2000–2001 Yellowstone array [Yuan and Dueker, 2005], the 1999–2000 Billings array [Yuan et al., 2008] and the 2000–2001 Stanford Snake River Plain axis array [Walker et al., 2004]. Teleseismic P wave arrivals for receiver function analysis were windowed from the continuous data for all events with body wave magnitudes >5.3 and the seismic recording components rotated into the vertical, radial, tangential coordinate system. To source normalize the events, a multitaper spectral correlation method was used [Park and Levin, 2000; Helffrich, 2006]. The vertical component was used as an estimate of the source function and deconvolved with a dynamic water level [Clayton and Wiggins, 1976] derived from the preevent noise spectral amplitude. The resulting receiver functions were then culled of noisy traces by removing the 20% of the radial component receiver function with RMS amplitudes greater than three times the mean of the data set. In addition, a visual inspection was done to remove dead and/or harmonic traces. Finally, all the radial receiver

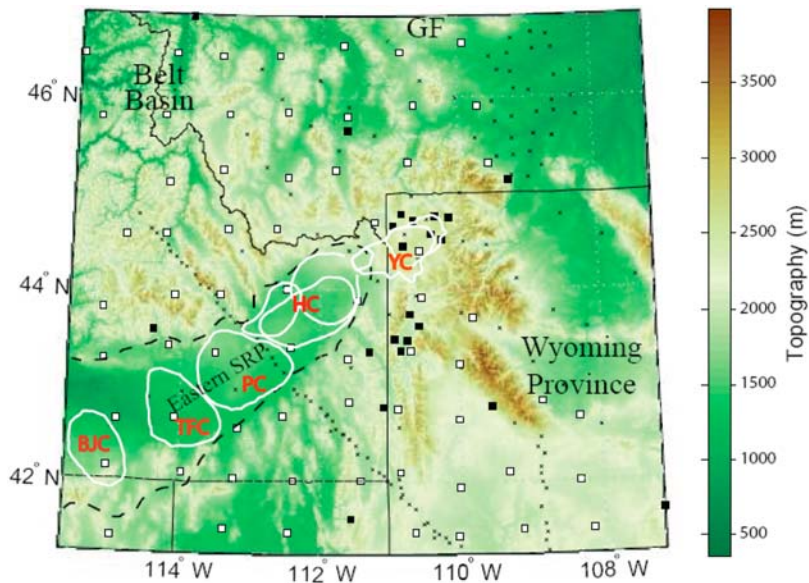


Figure 1. Seismic stations and topography. The eastern Snake River Plain is outlined with the black dashed line, and the volcanic calderas are denoted as white outlines with labels: 12.7–10.5 Ma Bruno-Jarbridge (BJC), 10–8.6 Ma Twin Fall (TFC), 10.1–10.3 Ma Picabo (PC), the 6.6–4.2 Ma Heise field (HC, a composite of at least three calderas), and the 2.1–0.6 Ma Huckleberry Ridge/Island Park/Yellowstone caldera (YC) field. Seismic stations used in this study are denoted as follows: transportable array stations (white squares), four PASSCAL experiment stations (crosses), and University of Utah/Grand Teton Park/National Seismic network stations (filled squares).

functions were linearly stacked with moveout corrections to provide 134 station stack traces (Figure 2).

[6] For each of the individual stations, a crustal thickness and bulk crustal V_p/V_s analysis (i.e., H-K analysis) is performed [Zandt *et al.*, 1995; Zhu and Kanamori, 2000] to constrain the mean crustal thickness and V_p/V_s value in the seismic sampling cone beneath each station (Figure 3). The weighting of S wave arrivals converted at the Moho in the H-K stacks is 0.6 (direct arrival), 0.3 (2p1s free surface reverberation), and 0.1 (2s1p free surface reverberation). The shear velocity at each station was specified to be the 1-D velocity profiles which were extracted at each station point (Figure 4) from the shear wave velocity tomogram [Stachnik *et al.*, 2008]. The V_p/V_s and crustal thickness marginal probability density functions were estimated using bootstrapping with replacement [Efron and Tibshirani, 1986]. The probability functions derived from the bootstrapping are generally peaked unimodal functions (Figures 3b and 3c): indicating reasonable resolution of the trade-off between crustal thickness and V_p/V_s variations. The best estimate of the two model parameters was considered to be the mode of the distributions. The parameter errors were estimated from these probability

functions by estimating the standard deviation about the mode of the probability function.

[7] To construct maps of the V_p/V_s (Figure 5), crustal thickness and crustal thickness errors (Figure 6), a least squares spline algorithm with a second derivative regularization term was used to interpolate the single-station results. The RMS difference between the spline predicted parameter values and the H-K measured crustal thickness and V_p/V_s values were small due to the spatial coherence of the single-station measurements. The crustal thickness errors (standard deviation) from bootstrapping the peak arrival time of the Moho arrival are <1.5 km (Figure 6b). However, this crustal thickness error estimate does not include the migration velocity model uncertainties associated with the shear wave velocity model (Figure 4) and the V_p/V_s map uncertainties used to migrate the receiver functions (Figure 5). Sensitivity analysis finds that a 0.2 km/s variation in the bulk shear velocity would produce a 0.5 km variation in Moho depth [Zhu and Kanamori, 2000]. Our surface wave based shear velocity tomogram is a well-resolved image and has errors <0.2 km/s for the mean crustal velocity [Stachnik *et al.*, 2008]; thus, the crustal thickness errors associated with our shear velocity tomogram migration velocities is estimated

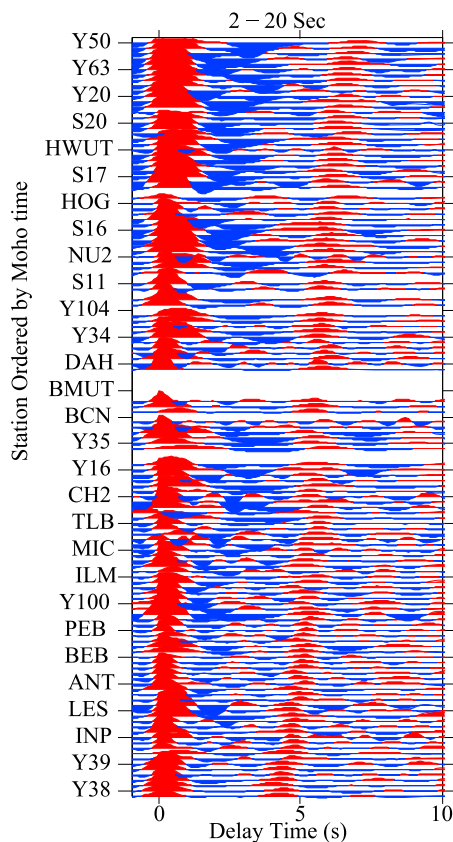


Figure 2. Station mean radial receiver functions for selected stations filtered at 2–20 s band pass. The receiver functions for each station were moveout corrected to 0.06 s/km ray parameter and linearly stacked. The stations are ordered by arrival time of the Moho arrival at 4.3–6.9 s.

as <1 km. Sensitivity analysis also shows that a 0.1 change in V_p/V_s will produce about a 4 km change in Moho depth [Zhu and Kanamori, 2000]. Our V_p/V_s error map (Figure A1) finds that the standard deviation of our bootstrapped V_p/V_s measurements is <0.03; thus, crustal thickness errors associated with our V_p/V_s map are estimated as <1.3 km. Assuming the three sources of error are independent, the maximum uncertainty in our crustal thickness maps is estimate as <3.7 km, more typically <2.5 km.

[8] The common conversion point (CCP) receiver function images [Dueker and Sheehan, 1997] were constructed using a three dimensional pixel parameterization with 2 km thick layers and 40 by 40 km wide CCP bins (Figures 8–11). The bin center points were spaced every 10 km so that adjacent bins had 75% data overlap, but no data overlap at three bin offsets. Time was mapped to depth using our shear velocity tomogram [Stachnik

et al., 2008] and the V_p/V_s map (Figure 5) for the crust. For the mantle below the Moho, the IASPEI91 velocity model mean upper mantle V_p/V_s value of 1.81 was used.

3. Results

3.1. Single-Station Interpolated Maps

[9] As our prior seismic results reported [Stachnik *et al.*, 2008], the mean crustal velocity map generally shows high (>3.6 km/s) mean velocity Wyoming province crust and low (<3.5 km/s) mean velocity Yellowstone caldera crust (Figure 4). The high-velocity Wyoming crust is primarily due to a high-velocity lower crustal layer imaged by the shear wave tomogram (Figure 11). This layer has been previously imaged as the so-called 7.x magmatic underplate layer (i.e., with a velocity >7.0 km/s) from active source studies [e.g., Gorman *et al.*, 2002]. In addition, the CCP images find a positive arrival from the top of this high-velocity layer where the station density is highest within the Billings, Montana array (Figures 8, 9, and 11).

[10] The V_p/V_s map (Figure 5) shows a reasonable range of 1.76–1.86 (ignoring the map edge values). The mean V_p/V_s is 1.81 compared to global estimate mean continental crustal value of 1.79 [Zandt and Ammon, 1995; Christensen, 1996]. A typical quality H-K analysis is shown in Figure 3 which finds a V_p/V_s value of 1.79 ± 0.02 . The maximum error in the V_p/V_s map is 0.03 as found by bootstrapping the H-K analysis. The principle anomaly observed in the V_p/V_s map is the relatively high values (>1.84) along the ESRP and normal values within the Yellowstone Park.

[11] The crustal thickness map (Figure 6a) generally shows thick crust (54–48 km) within the Wyoming province crust in Wyoming and eastern Montana. Specifically, thick crust is found beneath the Billings, Montana region and the two sampled Laramide age blocks associated with the Wind Rivers and Beartooth Mountains. But, the seismic sampling under the Bighorns Fault block is too sparse to draw any conclusions with respect to its crustal thickness. Three patches of intermediate thickness (40–44) crust are found within Wyoming surrounding the Wind River and Beartooth Laramie blocks. Thin crust (33–37 km) is found within the Montana Basin and Range Province [Zeiler *et al.*, 2005], beneath the sampled Idaho Batholith [Kuntz *et al.*, 2005], and to the south of the central ESRP. The Yellowstone Plateau region has crustal thick-

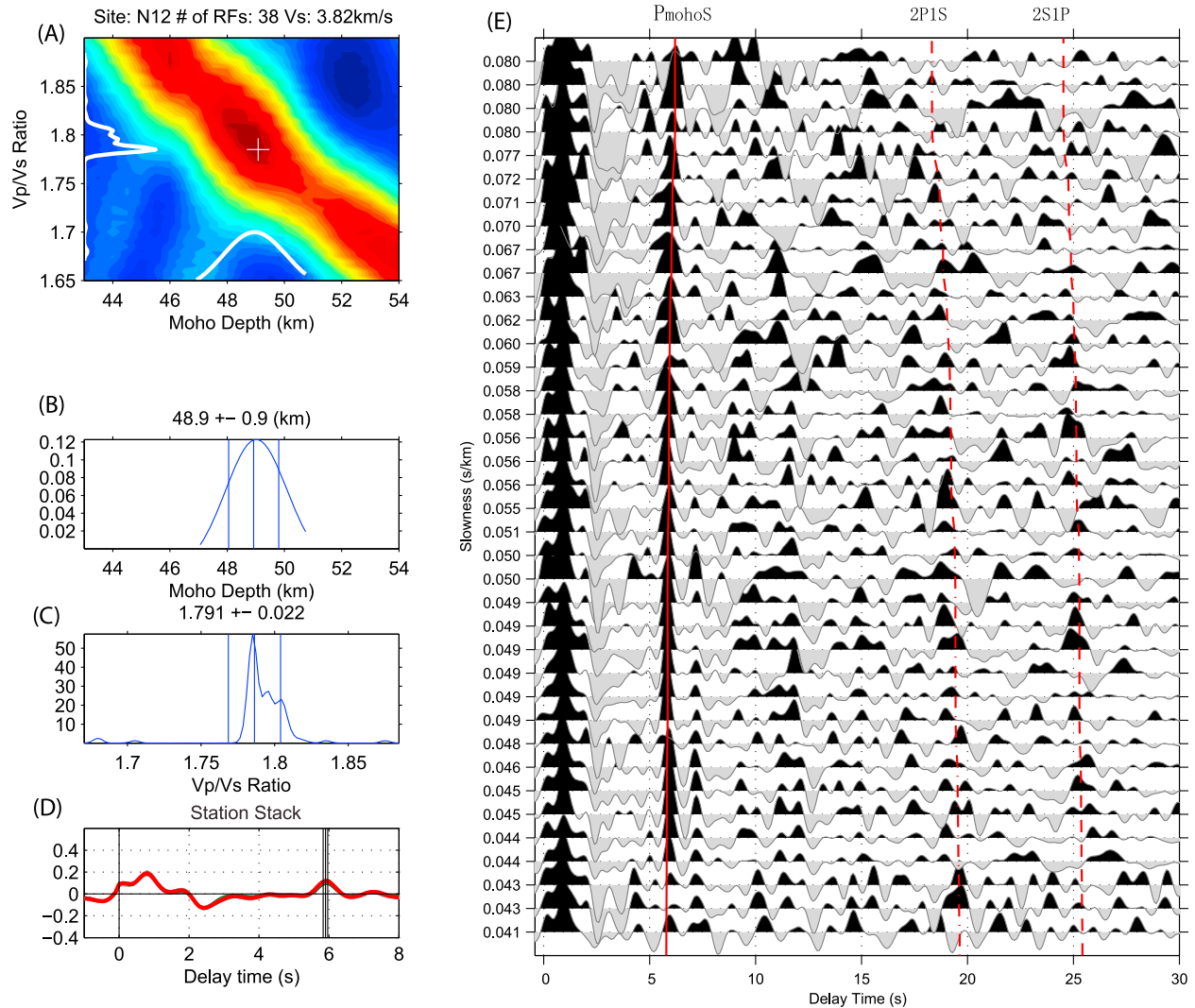


Figure 3. H-K stack analysis for a typical station. (a) H-K stack amplitude for the Moho depth versus V_p/V_s . The one-dimensional probability density function are the white lines along the x and y axes. (b) Estimate of Moho depth (distribution mode) and error as vertical bars. (c) Estimate of crustal V_p/V_s (distribution mode) and error as vertical bars. (d) Mean station moveout corrected radial receiver function. The Moho arrival is marked at 6 s, and amplitude is with respect to the vertical P wave component. (e) Station radial receiver function data with moveout curves for the direct (P_{mohoS}) and two free surface Moho reverberations (2P1S and 2S1P) overlaid.

ness of 47–52 km; this thick crust primarily manifests the Laramide age shortening associated with the Beartooth Mountains and the magmatic underplate that created the high-velocity lower crust beneath much of the Wyoming Province crust.

[12] The ESRP crustal thickness is found to thin by 8 km from 49 km at the NE end where the Huckleberry Ridge/Island Park calderas reside (Figure 7, cross section B) to 41 km beneath the SW end of our ESRP sampling where the Twin Falls caldera resides (Figure 7, cross sections F and G). The most remarkable crustal thickness anomaly observed in the ESRP perpendicular cross sections is a lobe of

thicker crust located beneath the NW ESRP margin adjacent to the Heise caldera field (Figure 7, cross sections C–E). The cross sections through this NW Heise crustal anomaly show 44–46 km crust extends 50–80 km to the NW of the ESRP margin. This NW Heise crustal anomaly contrasts with the cross sections through the older Picabo and Twin Fall calderas (cross sections F and G) where crustal thicknesses >38 km are confined within the ESRP physiographic margins. These reported ESRP crustal thickness values are generally consistent with refraction and local earthquake analysis [Smith *et al.*, 1982; Sparlin *et al.*, 1982; Sheriff and

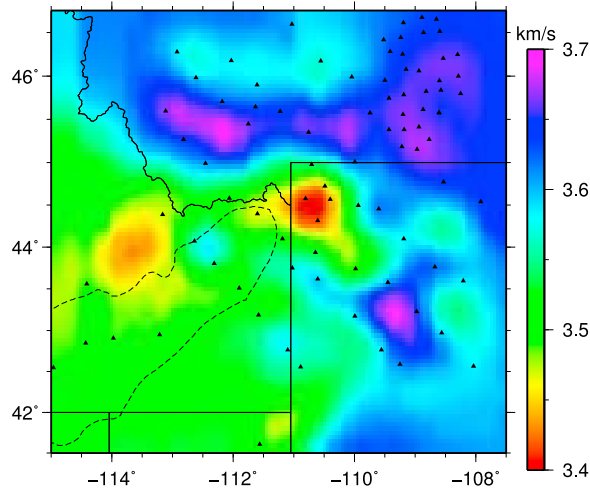


Figure 4. Mean crustal shear velocity from combined inversion of diffusive and ballistic surface wave dispersion measurements [Stachnik *et al.*, 2008]. PASSCAL stations used in this surface wave analysis are plotted as triangles.

Stickney, 1984; Henstock *et al.*, 1998; Zeiler *et al.*, 2005].

3.2. Common Conversion Point Images

[13] The CCP images (Figures 8–11) find that the direct Moho arrival is well imaged by migration of our radial receiver function data set. The ESRP/Yellowstone Plateau parallel cross section (Figure 8, cross section A) shows the Moho thickening to the NE toward the Yellowstone Plateau and thick crust within the Wyoming province. At the eastern end of this cross section, the top of the Wyoming Province high-velocity lower crustal layer is imaged at 35 km depth with the Moho at 52 km depth. The NW–SE cross section through the Yellowstone caldera (Figure 8, cross section B) shows a sharp change in crustal thickness at the NE corner of Yellowstone Park from thin crust beneath the Montana Basin and Range to thick crust beneath the Yellowstone caldera and the Wyoming province. The ESRP perpendicular cross section across the Picabo caldera (Figure 8, cross section C) shows thick Wyoming province crust at the SE end of the image and thin crust beneath the Montana Basin and Range province. The ESRP crust beneath the Picabo caldera is found to be seismically transparent with upper crustal structure outside the ESRP being truncated at the ESRP margins. In general, the ESRP Moho is depressed by 2–4 km with respect to the adjacent NW and SE margins (see also Figure 7).

[14] The E–W Montana/northern Idaho cross section (Figure 8, cross section D) shows the greatest crustal thickness variation from 52 km beneath eastern Montana to 35 km near the Eocene age Bitterroot detachment and granitic batholith in northern Idaho [Foster *et al.*, 2001]. The top of the high-velocity lower crustal layer is also found at the east end of this cross section. The N–S Wyoming/Montana cross section (Figure 8, cross section E) shows the thick (48–52 km) crust beneath the region shortening during the Laramide orogeny and not affected by late Cenozoic extension [Dickinson, 2004]. The top of the high-velocity lower crustal layer is imaged north of 44.5° latitude beneath the Billings array (Figure 1). Two cross sections through the Billings array (Figure 9) show the direct Moho arrivals from the top of the high-velocity lower crustal layer at 28–34 km depth. The thickness of this lower crustal layer is up to 17 km thick with the layer thinning to zero thickness at the NE and SW end of cross section B.

[15] A final notable feature in the CCP images is a paired positive and negative amplitude arrival at 12 and 18 km depth beneath the Yellowstone caldera (Figures 8 (cross sections A and B) 10). This paired arrival would be consistent with a low-velocity

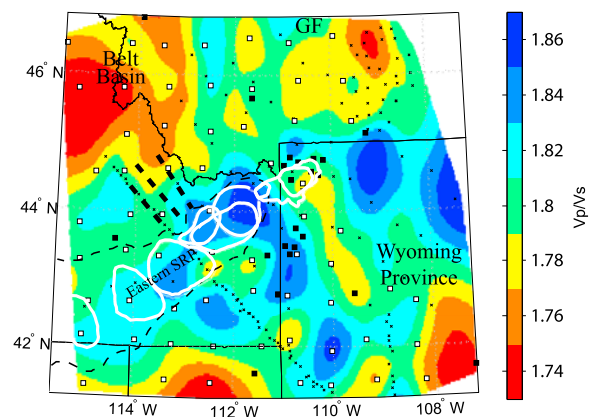


Figure 5. Crustal V_p/V_s map from interpolation of single-station H-K analysis results (i.e., Figure 3). The calderas are outlined with white solid lines, and the eastern Snake River Plain is outlined with the black dashed line. Stations are denoted as follows: transportable array stations (squares), PASSCAL experiment stations (dots), and University of Utah/Teton/National Seismic network stations (filled squares). The three dashed black lines to the NW of the Heise caldera field approximately locate the Beaverhead, Lemhi, and Lost River normal faults.

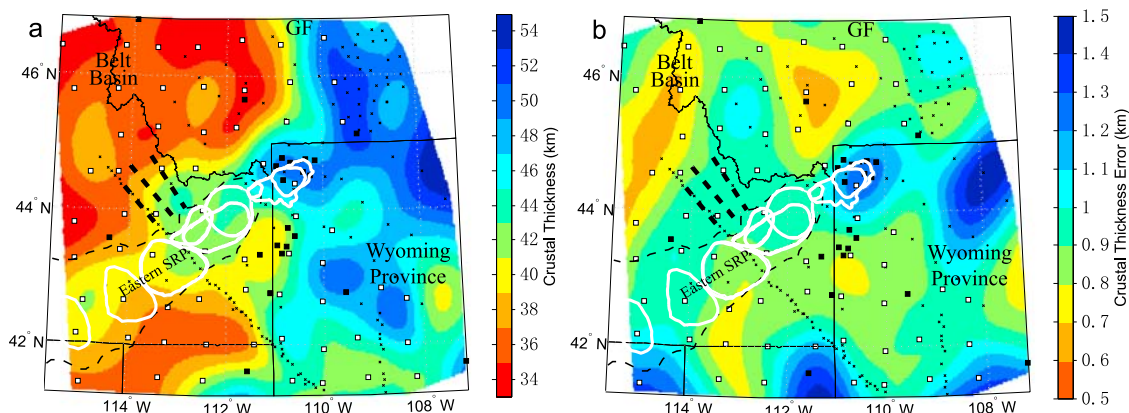


Figure 6. Crustal thickness and error map. (a) The calderas are outlined with white solid lines, and the eastern Snake River Plain is outlined with the black dashed line. Stations are denoted as follows: transportable array stations (squares), PASSCAL stations (dots), and University of Utah/Teton/National Seismic network stations (filled squares). (b) Crustal thickness standard deviation errors estimated via bootstrapping of the H-K analysis. This error analysis ignores velocity migration errors associated with the mean crustal shear velocity model (Figure 4) and the V_p/V_s map (Figure 5). The velocity migration uncertainties are assessed in section 2. The calderas are outlined with white solid lines, and the eastern Snake River Plain is outlined with the black dotted line.

zone: the 12 km negative polarity arrival manifesting a negative velocity gradient and the 18 km positive polarity arrival manifesting a positive velocity gradient. This paired arrival is directly under the two most volcanically active regions of the

Yellowstone caldera between the Mallard Lake and Sour creek resurgent Rhyolitic domes [Lowenstern and Hurwitz, 2008]. A similar finding of an upper crustal low-velocity zone is found by waveform modeling of teleseismic S wave data from three

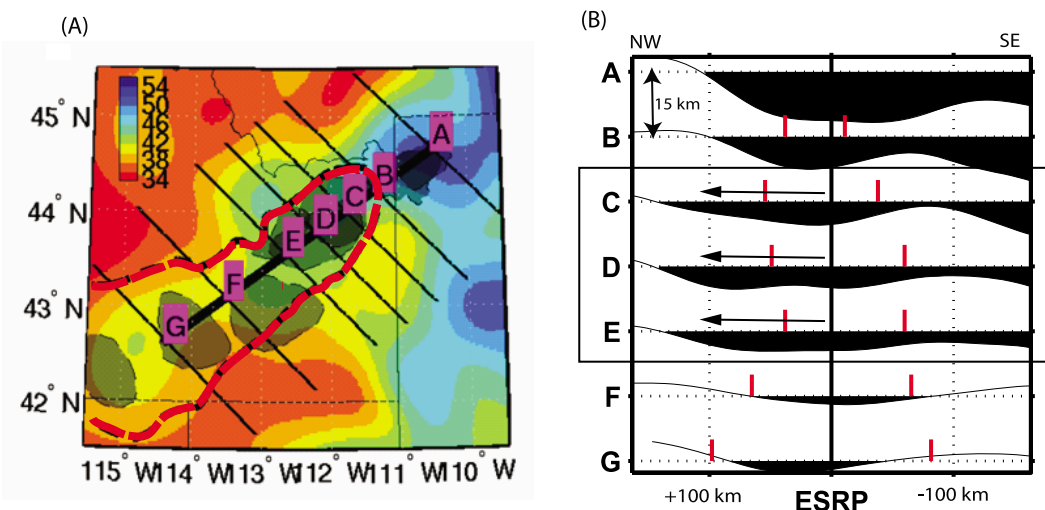


Figure 7. Eastern Snake River Plain crustal thickness maps and graphs. (a) The crustal thickness is indicated by the color bar. The cross sections shown in Figure 7b are labeled A–G, and the dark line down the center of the ESRP shows the zero values for the x axis coordinates in Figure 7b. The calderas are outlined as the gray shaded areas, and the eastern Snake River Plain is outlined with the black dashed line. (b) Crustal thickness graphs for cross sections A–G. The edge of the ESRP is marked by short red lines. The zero line for each graph is at 38 km depth, and a 15 km thickness variation is indicated by the scale bar. Cross sections C–E are boxed to indicate where the crust to the NW of the ESRP is anomalously thick with respect to cross sections F and G. The NW directed arrows indicated the direction of proposed lower crustal flow from beneath the Heise caldera field.

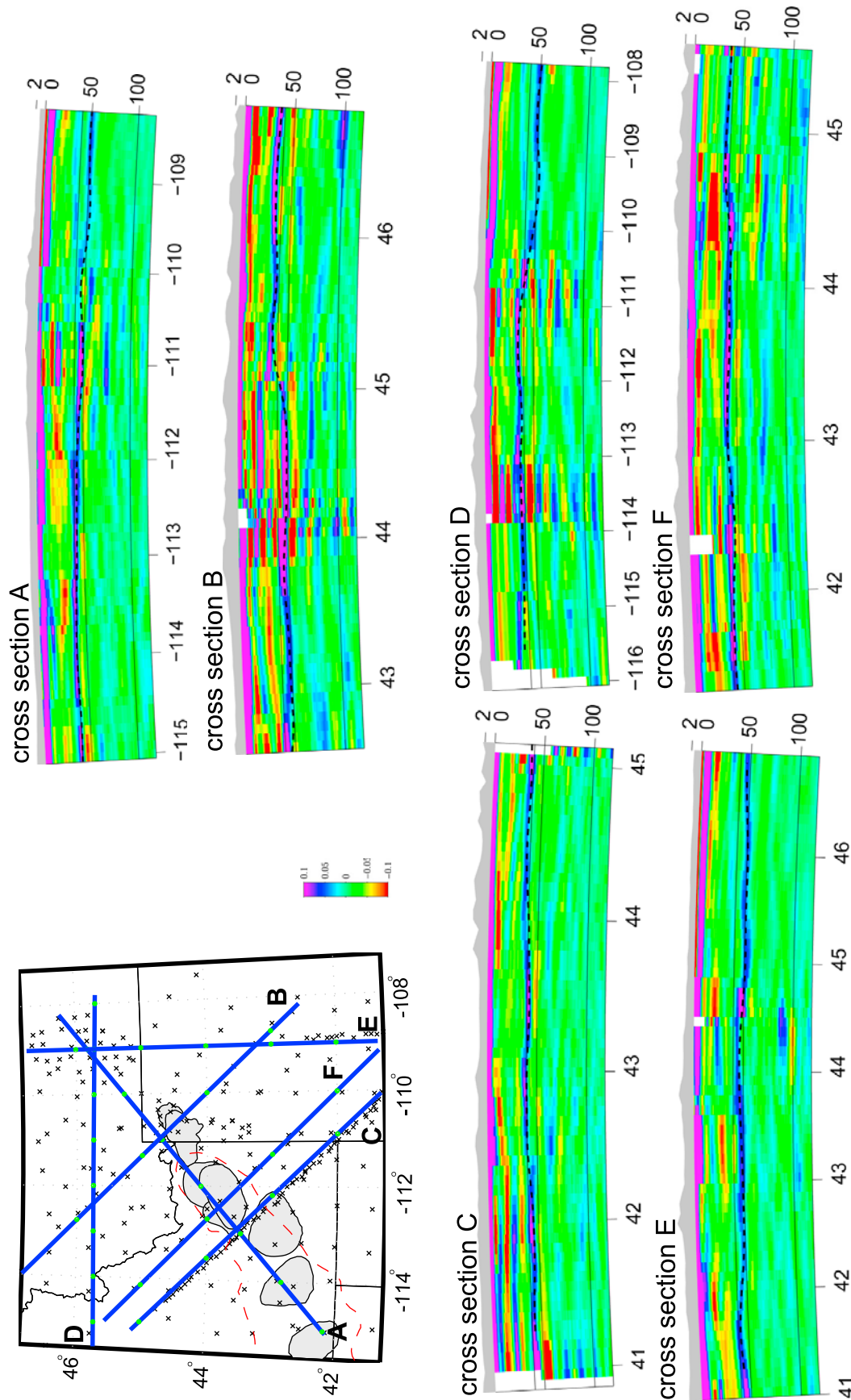


Figure 8. Common conversion point images. Topography is indicated as gray shading at the top of each section. Moho is indicated as black dotted line. Scale bar shows amplitude of positive (blue) and negative polarity (red) arrivals. Cross section A is the ESRP parallel section. Cross section B is the ESRP perpendicular section through Yellowstone Caldera. Cross section C is the ESRP perpendicular section through the Picabo caldera. Cross section D is the E-W section through Montana and northern Idaho. Cross section E is the N-S Wyoming province section. Cross section F is the ESRP perpendicular section through the Heise caldera field.

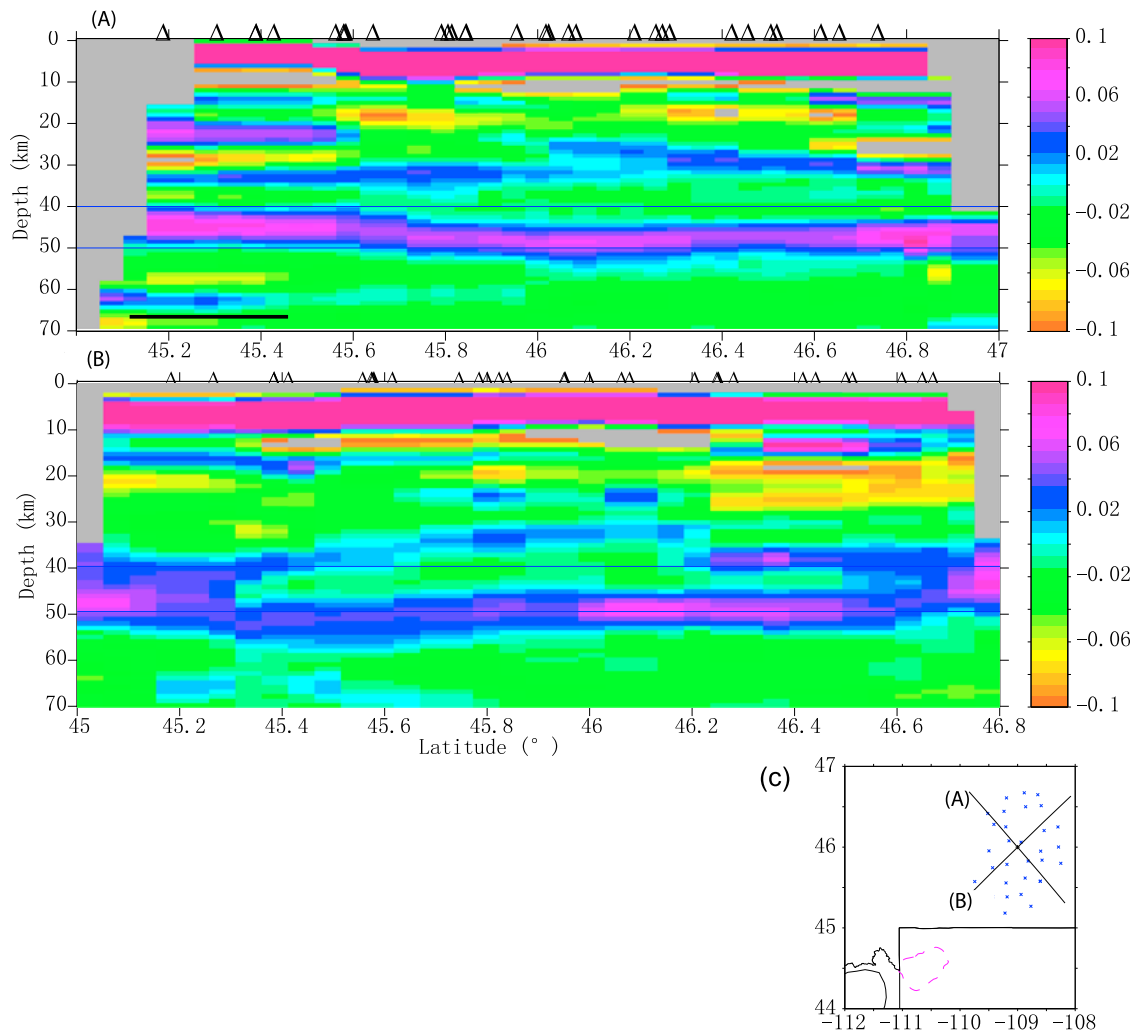


Figure 9. Billings array area common conversion point images. (a) Cross section A. (b) Cross section B. Note the positive arrival (blue-purple) that is found at 0–18 km above the Moho arrival at 47–52 km depth. (c) The locations of the cross sections and stations.

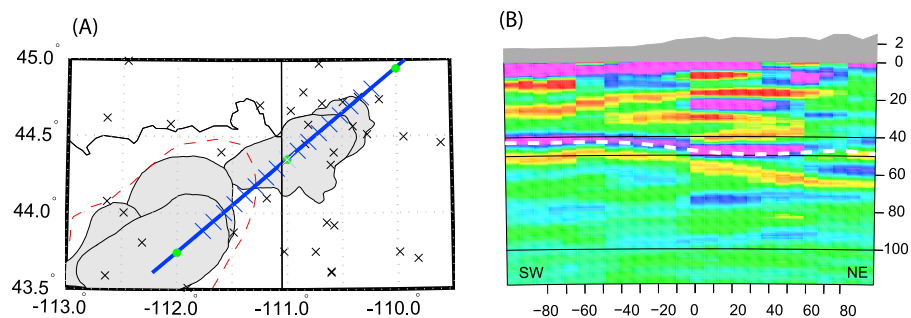


Figure 10. ESRP parallel common conversion point image highlighting structure under Yellowstone Caldera. (a) Cross section with calderas gray shaded and the ESRP outlined by the red dotted line. (b) Common conversion point image. Topography is indicated as gray shading at top of image, and the Moho is indicated as white dotted line.

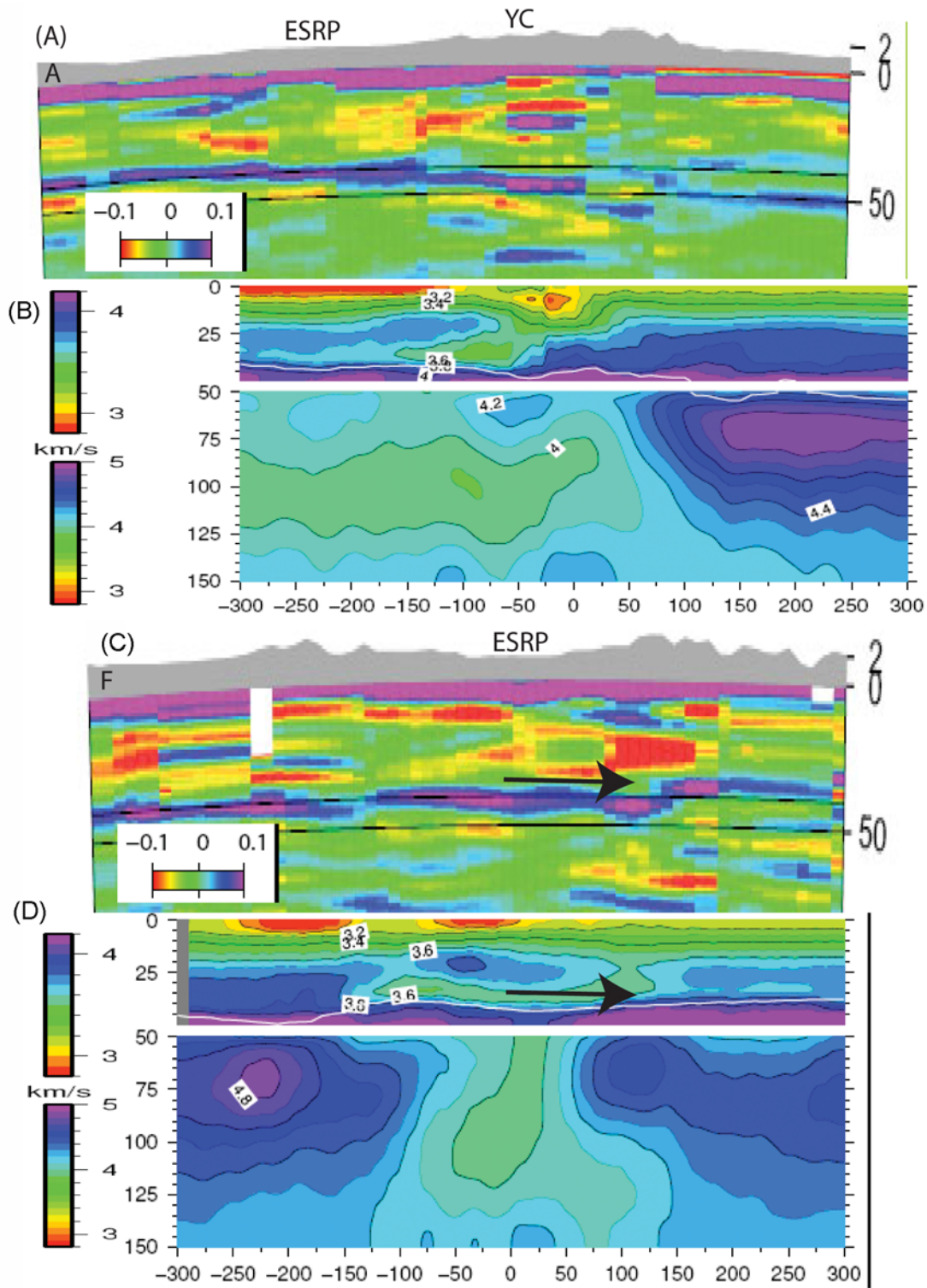


Figure 11. Coincident shear velocity tomogram [Stachnik *et al.*, 2008] and common conversion point images. The locations of cross sections A and F are shown in Figure 8. The gray shading at the top of each subplot is the elevation. The color scale for the CCP images denotes positive (blue) and negative polarity (red) arrivals. The color scale for the shear velocity is shown for the crust and mantle panels and the white line in the velocity images is the Moho. (a) CCP cross section A and (b) shear velocity tomogram. (c) CCP cross section F and (d) shear velocity tomogram. The arrows indicate the inferred dominant direction of lower crustal flow from beneath the Heise caldera field into the lower crust to the NW of the ESRP.



Yellowstone Park broadband stations [Chu *et al.*, 2009].

4. Discussion

4.1. Lower Crustal ESRP Outflow

[16] Our most important new result is our new crustal thickness map which provides a synoptic scale sufficient to assess the mass balances associated with the magmatic inflation of the ESRP crust and potential lower crustal outflow forced by the midcrustal densification caused by this magmatic load. If the hypothesis that magmatic injection along the ESRP has stimulated crustal flow is correct, then the time history of the crustal flow should be correlated with the magmatic injection history and the postcaldera lower crustal thermal evolution which controls viscosity. Given the high (>90 mW/m²) heat flow along the ESRP and its margins [Blackwell and Richards, 2004] and the finding of low flexural rigidity [Lowry and Smith, 1995; Lowry *et al.*, 2000], it seems plausible that the lower crust is capable of flow driven by the midcrustal sill load. Estimates of lower crustal flow rates of 1–7 cm/yr (10–70 km/Myr) in regions of elevated heat flow have been proposed where sufficient pressure gradients in the lower crust exist [Buck, 1991; Royden *et al.*, 1997, 2008]. Dividing the 50–80 km lateral extent of the anomalously thick crust to the NW of the Heise caldera field by the mean age of the Heise caldera field (5 Ma) provides a maximal lower crustal flow rate of about 1 cm/yr (10 km/Myr).

[17] The simplest crustal thickness evolution scenario for the ESRP and its margins assumes that prior to formation of the hot spot track, the crustal thickness and density structure was uniform perpendicular to the ESRP between the Twin Falls and Heise calderas and its adjacent margins. In addition, post-hot spot track integrated crustal dilatation is also assumed to be relatively uniform perpendicular to the ESRP. Estimates of net dilatation at the NW and SE ESRP margins is estimated as 15% and 25% [Rodgers *et al.*, 2002]. Thus, to first order, we assume that the ESRP initial conditions and integrated dilatation perpendicular to the ESRP have been relatively uniform. Given these assumptions, the only change in the ESRP crustal thickness with respect to its margins would result from mass additions due to magmatism and sedimentation or mass subtractions associated with caldera eruption atmospheric plumes. The sedimentation addition is estimated as <1 km and the atmospheric losses as

<0.75 km [Rodgers and McCurry, 2009]. These two effects are opposite in sign and nearly cancel; thus, the dominant ESRP mass variable is the caldera forming crustal magmatic injections. In summary, the expected thickening of the ESRP crust with respect to its margins is dictated by the petrologic and caldera heat budget constraints that suggest 8–14 km of mantle derived basaltic magmas are required to fuel the calderas [Hanan *et al.*, 2008; McCurry and Rodgers, 2009; Leeman *et al.*, 2008].

[18] The shear velocity tomogram finds a high-velocity (>3.6 km/s contour) midcrustal layer within the ESRP that starts at the NE end of the ESRP beneath the Island Park caldera and extends to the edge of our surface wave velocity sampling at the Picabo caldera (Figures 11a and 11b). Beneath the Heise caldera field, the 3.6 km/s shear velocity contour that outlines this layer resides between 18–32 km depth (14 km thick). At the SE end of the ESRP, the top of this high-velocity midcrustal layer deepens by about 5 km. This layer is thought to manifest the midcrustal sill (MCS) complex that forms the mafic magmatic “tanks” from whence the Rhyolitic caldera magmas were derived via fractionation, assimilation, and hybridization. Beneath this MCS layer, a relatively low velocity lower crustal “wedge” is found that is thickest beneath the Island Park caldera and pinches out at the SW edge of the Heise caldera field.

[19] The ESRP perpendicular cross section (Figures 11c and 11d) shows two interesting features: the MCS layer dips to the NW and the low-velocity (<3.6 km/s) lower crust extends up to 50 km to either side of the ESRP margins. With respect to the mantle velocity anomalies shown in the tomograms, the ESRP-YP physiographic province is underlain by very low (4 km/s) shear velocities at 75–125 km depth with a relatively high velocity mantle lid between the Moho and 75 km depth (Figures 11a and 11b). The low ESRP mantle velocity rapidly changes beneath the Beartooth Mountains to cratonic lithospheric velocity values of 4.9 km/s [Artemieva, 2009; Bedle and van der Lee, 2009]. In the ESRP perpendicular cross section (Figures 11c and 11d), the low-velocity ESRP mantle is found directly beneath the 90 km wide ESRP with higher-velocity mantle lithosphere beneath SW Wyoming (SE end) and western Montana (NW end).

[20] Based on the above observations, we believe a good circumstantial case is made for the flow of magmatically thickened lower crust from beneath

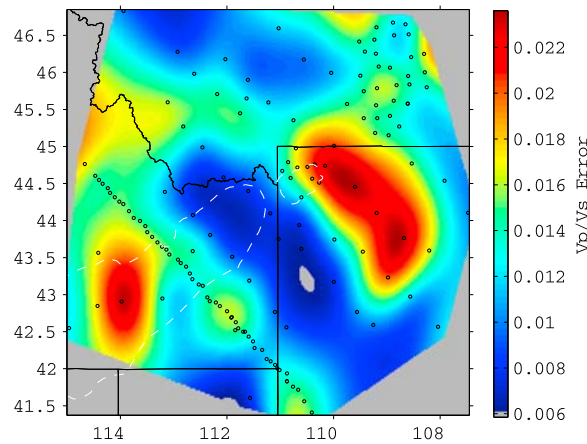


Figure A1. V_p/V_s map of standard deviation. The standard deviation was calculated via bootstrap resampling of the H-K analysis to calculate an ensemble of V_p/V_s and crustal thickness values.

the Heise caldera field into the adjacent NW margin crust. However, this statement begs the question of where the magmatically thickened ESRP crust has flowed from beneath the older Twin Falls and Picabo caldera fields. Two differences are noted between the Heise caldera field and the older Twin Falls and Picabo calderas. First, these two older calderas are spaced farther apart along the ESRP (Figure 1) indicating less mass flux into the ESRP per unit area. Second, these caldera fields have had more integrated dilatation with respect to the Heise caldera field because extension associated with caldera formation began earlier in this region [Anders *et al.*, 1989; Pierce and Morgan, 1992]. In addition, the proximity of these older calderas to the concentrated extension of the western Snake River Plain graben [Cummings *et al.*, 2000] and the Northern Nevada Rift [Glen and Ponce, 2002] is noted; these regions of concentrated extension could create lateral pressure gradients in the lower crust that would promote the flow of lower crustal mass from the magmatically thickened calderas areas.

4.2. Yellowstone Caldera Low-Velocity Zone

[21] Modern day gas fluxes near recent intracaldera basaltic eruptions [Lowenstern and Hurwitz, 2008] and deformation monitoring [Chang *et al.*, 2007; Puskas *et al.*, 2007] suggest that ongoing post 0.6 Ma Yellowstone caldera magmatic activity is occurring. The paired negative/positive amplitude arrivals at 12–18 km depth found beneath the Yellowstone caldera by the CCP images (Figures 8 (cross sections A and B) and 10) are consistent with other

geophysical data that suggest the Yellowstone caldera low-velocity and low-density anomalies extend to about 20 km depth: the low velocities beneath the caldera in our shear wave tomogram (Figures 11a and 11b) and gravity modeling [DeNosaquo *et al.*, 2010]. A tomogram constructed from measured local earthquake traveltimes finds a low (5.4 km/s) P wave velocity at 8 km depth, but cannot resolve structure below 12 km depth [Husen *et al.*, 2004]. Waveform modeling of S-P precursors from three broadband stations near the Mallard Lake dome requires a substantial low-velocity zone at 5–8 km with a thickness of 3–5 km [Chu *et al.*, 2009]. Thus, our finding of a 6 km thick low-velocity zone with its top at 12 km depth provides a depth range over which basaltic magma is being staged beneath the Yellowstone caldera. In the near future, this finding can be tested via higher-resolution ambient noise surface wave imaging with the deployment of new broadband seismometers within Yellowstone Park in 2010.

Appendix A

[22] Map of the standard deviation of V_p/V_s measurements (Figure A1) finds an average of 0.015. The V_p/V_s errors were estimated for each station via bootstrap resampling of the peak amplitude of the H-K image. These individual station standard deviation estimates are interpolated using a two-dimensional spline that fits the individual station error estimates to within their individual error bars.

Acknowledgments

[23] This research was support by the National Science Foundation Geophysics program grant 0440432. The seismic data collection was supported by the IRIS-PASSCAL and EARTHSCOPE NSF facilities.

References

- Anders, M. (2009), Neogene tephra correlations in eastern Idaho and Wyoming: Implications for Yellowstone hotspot-related volcanism and tectonic activity, *Geol. Soc. Am. Bull.*, *121*, 837–856, doi:10.1130/B26300.1.
- Anders, M. H., and N. H. Sleep (1992), Magmatism and extension: The thermal and mechanical effects of the Yellowstone hotspot, *J. Geophys. Res.*, *97*(B11), 15,379–15,393, doi:10.1029/92JB01376.
- Anders, M. H., J. W. Geissman, L. A. Piety, and T. J. Sullivan (1989), Parabolic distribution of circumeastern Snake River Plain seismicity and latest Quaternary faulting: Migratory pattern and association with the Yellowstone hotspot, *J. Geophys. Res.*, *94*(B2), 1589–1621, doi:10.1029/JB094iB02p01589.



- Artemieva, I. M. (2009), The continental lithosphere: Reconciling thermal, seismic, and petrologic data, *Lithos*, 109(1–2), 23–46, doi:10.1016/j.lithos.2008.09.015.
- Bedle, H., and S. van der Lee (2009), *S* velocity variations beneath North America, *J. Geophys. Res.*, 114, B07308, doi:10.1029/2008JB005949.
- Blackwell, D. D., and M. Richards (2004), *Geothermal Map of North America*, Am. Assoc. of Pet. Geol., Tulsa, Okla.
- Bonnichsen, B., W. P. Leeman, N. Honjo, W. C. McIntosh, and M. Godchaux (2007), Miocene Silicic volcanism in southwestern Idaho: Geochronology, geochemistry, and evolution of the central Snake River Plain, *Bull. Volcanol.*, 70, 315–342, doi:10.1007/s00445-007-0141-6.
- Buck, W. R. (1991), Modes of continental lithospheric extension, *J. Geophys. Res.*, 96(B12), 20,161–20,178, doi:10.1029/91JB01485.
- Chang, W., R. B. Smith, C. Wicks, J. M. Farrell, and C. M. Puskas (2007), Accelerated uplift and magmatic intrusion of the Yellowstone Caldera, 2004–2006, *Science*, 318, 952–956, doi:10.1126/science.1146842.
- Christensen, N. I. (1996), Poisson's ratio and crustal seismology, *J. Geophys. Res.*, 101(B2), 3139–3156, doi:10.1029/95JB03446.
- Chu, R., D. Sun, and D. V. Helmberger (2009), Shallow structure beneath the Yellowstone caldera, paper presented at Annual Meeting, EarthScope, Boise, Idaho.
- Clayton, R. W., and R. A. Wiggins (1976), Source shape estimation and deconvolution of teleseismic body waves, *Geophys. J. R. Astron. Soc.*, 47, 151–177.
- Cummings, M. L., J. G. Evans, M. L. Forns, and K. R. Lees (2000), Stratigraphic and structural evolution of the middle miocene synvolcanic Oregon-Idaho graben, *Geol. Soc. Am. Bull.*, 112(5), 668–682, doi:10.1130/0016-7606(2000)112<0668:SASEOT>2.3.CO;2.
- DeNosaquo, K. R., R. B. Smith, and A. Lowry (2010), Density and lithospheric strength models of the Yellowstone-Snake River Plain volcanic system from gravity and heat flow data, *J. Volcanol. Geotherm. Res.*, 188, 108–127.
- Dickinson, W. R. (2004), Evolution of the North American Cordillera, *Annu. Rev. Earth Planet. Sci.*, 32(1), 13–45, doi:10.1146/annurev.earth.32.101802.120257.
- Dickinson, W. R. (2006), Geotectonic evolution of the Great Basin, *Geosphere*, 2(7), 353–368, doi:10.1130/GES00054.1.
- Dueker, K. G., and A. F. Sheehan (1997), Mantle discontinuity structure from midpoint stacks of converted P and S waves across the Yellowstone hotspot track, *J. Geophys. Res.*, 102(B4), 8313–8327, doi:10.1029/96JB03857.
- Dueker, K., and H. Yuan (2004), Upper mantle P-wave velocity structure from PASSCAL teleseismic transects across Idaho, Wyoming and Colorado, *Geophys. Res. Lett.*, 31, L08603, doi:10.1029/2004GL019476.
- Efron, B., and R. Tibshirani (1986), Bootstrap methods for standard errors, confidence intervals, and other measures of statistical accuracy, *Stat. Sci.*, 1, 54–77, doi:10.1214/ss/1177013815.
- Foster, D. A., C. Schafer, C. M. Fanning, and D. W. Hyndman (2001), Relationships between crustal partial melting, plutonism, orogeny, and exhumation: Idaho-Bitterroot batholith, *Tectonophysics*, 342(3–4), 313–350, doi:10.1016/S0040-1951(01)00169-X.
- Foster, D. A., P. A. Mueller, D. W. Mogk, J. L. Wooden, and J. J. Vogl (2006), Proterozoic evolution of the western margin of the Wyoming craton: Implications for the tectonic and magmatic evolution of the northern Rocky Mountains, *Can. J. Earth Sci.*, 43(10), 1601–1619, doi:10.1139/E06-052.
- Glen, J. M. G., and D. A. Ponce (2002), Large-scale fractures related to inception of the Yellowstone hotspot, *Geology*, 30(7), 647–650, doi:10.1130/0091-7613(2002)030<0647:LSFRTI>2.0.CO;2.
- Gorman, A. R., et al. (2002), Deep Probe: Imaging the roots of western North America, *Can. J. Earth Sci.*, 39, 375–398.
- Hamilton, W. B. (1989), Crustal geologic processes of the United States, in *Geophysical Framework of the Continental United States*, edited by L. C. Pakiser and W. D. Mooney, *Mem. Geol. Soc. Am.*, 172, 743–781.
- Hanan, B. B., J. W. Shervais, and S. K. Vetter (2008), Yellowstone plume continental lithosphere interaction beneath the Snake River Plain, *Geology*, 36(1), 51–54, doi:10.1130/G23935A.1.
- Helffrich, G. (2006), Extended-time multitaper frequency domain cross-correlation receiver-function estimation, *Bull. Seismol. Soc. Am.*, 96(1), 344–347, doi:10.1785/0120050098.
- Henstock, T. J., K. C. Miller, S. H. Harder, A. R. Gorman, R. M. Clowes, M. J. A. Burianyk, E. D. Humphreys, A. Levander, C. M. Snelson, and G. R. Keller (1998), Probing the Archean and Proterozoic lithosphere of western North America, *GSA Today*, 8(7), 1–5.
- Hildreth, W., and S. Moorbath (1988), Crustal contributions to arc magmatism in the Andes of central Chile, *Contrib. Mineral. Petrol.*, 98(4), 455–489, doi:10.1007/BF00372365.
- Husen, S., R. B. Smith, and G. Waite (2004), Evidence for gas and magmatic sources beneath the Yellowstone volcanic field from seismic tomography, *J. Volcanol. Geotherm. Res.*, 131, 397–410.
- Kuntz, M. A., L. W. Snee, and D. A. Unruh (2005), Temporal, compositional, and structural development of the Idaho batholith near McCall, Idaho, *Geochim. Cosmochim. Acta*, 69(10), A249.
- Leeman, W. P., C. Annen, and J. Dufek (2008), Snake River Plain-Yellowstone silicic volcanism: Implications for magma genesis and magma fluxes, in *Dynamics of Crustal Magma Transfer, Storage, and Differentiation—Integrating Geochemical and Geophysical Constraints*, *Geol. Soc. Spec. Publ.*, 304, 235–259, doi:10.1144/SP304.12.
- Lowenstern, J. B., and S. Hurwitz (2008), Monitoring a supervolcano in repose: Heat and volatile flux at the Yellowstone Caldera, *Elements*, 4, 35–40, doi:10.2113/GSELEMENTS.4.1.35.
- Lowry, A. R., and R. B. Smith (1995), Strength and rheology of the western U.S. Cordillera, *J. Geophys. Res.*, 100(B9), 17,947–17,963, doi:10.1029/95JB00747.
- Lowry, A. R., N. M. Ribe, and R. B. Smith (2000), Dynamic elevation of the Cordillera, western United States, *J. Geophys. Res.*, 105(B10), 23,371–23,390, doi:10.1029/2000JB900182.
- McCurry, M., and D. Rodger (2009), Mass transfer along the Yellowstone hot spot track I: Petrologic constraints on the volume of mantle-derived magma, *J. Volcanol. Geotherm. Res.*, 188, 86–98, doi:10.1016/j.volgeo.2009.04.001.
- McQuarrie, N., and D. W. Rodgers (1998), Subsidence of a volcanic basin by flexure and lower crustal flow: The eastern Snake River Plain, Idaho, *Tectonics*, 17, 203–220, doi:10.1029/97TC03762.
- Park, J., and V. Levin (2000), Receiver functions from multitaper spectral correlation estimates, *Bull. Seismol. Soc. Am.*, 90(6), 1507–1520, doi:10.1785/0119990122.
- Perkins, M. E., and B. P. Nash (2002), Explosive silicic volcanism of the Yellowstone hotspot: The ash fall tuff record, *Geol. Soc. Am. Bull.*, 114(3), 367–381, doi:10.1130/0016-7606(2002)114<0367:ESVOTY>2.0.CO;2.



- Pierce, K. L., and L. A. Morgan (1992), The track of the Yellowstone hotspot: Volcanism, faulting, and uplift, in *Regional Geology of Eastern Idaho and Western Wyoming, Mem. Geol. Soc. Am.*, 179, 1–53.
- Puskas, C. M., R. B. Smith, C. M. Meertens, and W. L. Chang (2007), Crustal deformation of the Yellowstone–Snake River Plain volcano–tectonic system: Campaign and continuous GPS observations, 1987–2004, *J. Geophys. Res.*, 112, B03401, doi:10.1029/2006JB004325.
- Rodgers, D. W., and M. McCurry (2009), Mass transfer along the Yellowstone hotspot track II: Kinematic constraints on the volume of mantle-derived magma, *J. Volcanol. Geotherm. Res.*, 188, 99–107, doi:10.1016/j.jvolgeores.2009.05.014.
- Rodgers, D., H. Ore, R. Bobo, N. McQuarrie, and N. Zentner (2002), Extension and subsidence of the eastern Snake River Plain, in *Tectonic and Magmatic Evolution of the Eastern Snake River Plain, Idaho Geol. Surv. Bull.*, 30, pp. 121–160, Idaho Geol. Surv., Moscow.
- Royden, L. H., B. Burchfiel, R. W. King, E. Wang, Z. Chen, F. Shen, and Y. Liu (1997), Surface deformation and lower crustal flow in eastern Tibet, *Science*, 276(5313), 788–790, doi:10.1126/science.276.5313.788.
- Royden, L. H., B. Burchfiel, and R. D. van der Hilst (2008), The geologic evolution of the Tibetan Plateau, *Science*, 321, 1054–1058, doi:10.1126/science.1155371.
- Saltzer, R. L., and E. D. Humphreys (1997), Upper mantle P wave velocity structure of the eastern Snake River plain and its relationship to geodynamic models of the region, *J. Geophys. Res.*, 102(B6), 11,829–11,841, doi:10.1029/97JB00211.
- Sheriff, S. D., and M. C. Stickney (1984), Crustal structure of southwestern Montana and east-central Idaho: Results of a reversed seismic refraction line (USA), *Geophys. Res. Lett.*, 11(4), 299–302, doi:10.1029/GL011i004p00299.
- Smith, R. B., M. Schilly, L. W. Braile, J. Ansorge, J. L. Lehman, M. R. Baker, C. Prodehl, J. H. Healy, S. Mueller, and R. W. Greensfelder (1982), The 1978 Yellowstone–Eastern Snake River Plain seismic profiling experiment: Crustal structure of the Yellowstone region and experiment design, *J. Geophys. Res.*, 87(B4), 2583–2596, doi:10.1029/JB087iB04p02583.
- Sparlin, M. A., L. W. Braile, and R. B. Smith (1982), Crustal structure of the eastern Snake River Plain from ray trace modeling of seismic refraction data, *J. Geophys. Res.*, 87, 2619–2633, doi:10.1029/JB087iB04p02619.
- Stachnik, J. C., K. Dueker, D. L. Schutt, and H. Yuan (2008), Imaging Yellowstone plume–lithosphere interactions from inversion of ballistic and diffusive Rayleigh wave dispersion and crustal thickness data, *Geochem. Geophys. Geosyst.*, 9, Q06004, doi:10.1029/2008GC001992.
- Walker, K. T., G. Bokelmann, and L. Klemperer Simon (2004), Shear wave splitting reveals a mantle upwelling beneath eastern Nevada, *Earth Planet. Sci. Lett.*, 222, 529–542, doi:10.1016/j.epsl.2004.03.024.
- Yuan, H., and K. Dueker (2005), Teleseismic P-wave tomogram of the Yellowstone plume, *Geophys. Res. Lett.*, 32, L07304, doi:10.1029/2004GL022056.
- Yuan, H., K. Dueker, and D. L. Schutt (2008), Testing five of the simplest upper mantle anisotropic velocity parameterizations using teleseismic S and SKS data from the Billings, Montana PASSCAL array, *J. Geophys. Res.*, 113, B03304, doi:10.1029/2007JB005092.
- Zandt, G., and C. J. Ammon (1995), Continental crust composition constrained by measurements of crustal Poisson’s ratio, *Nature*, 374(6518), 152–154, doi:10.1038/374152a0.
- Zandt, G., S. C. Myers, and T. C. Wallace (1995), Crust and mantle structure across the Basin and Range–Colorado Plateau boundary at 37°N latitude and implications for Cenozoic extensional mechanism, *J. Geophys. Res.*, 100, 10,529–10,548, doi:10.1029/94JB03063.
- Zeiler, C. P., M. C. Stickney, and M. A. Speece (2005), Velocity structure of western Montana, *Bull. Seismol. Soc. Am.*, 95(2), 759–762, doi:10.1785/0120040088.
- Zhu, L. P., and H. Kanamori (2000), Moho depth variation in southern California from teleseismic receiver functions, *J. Geophys. Res.*, 105(B2), 2969–2980, doi:10.1029/1999JB900322.